Optical Fiber Technology 90 (2025) 104136

Contents lists available at ScienceDirect

Optical Fiber Technology

journal homepage: www.elsevier.com/locate/yofte

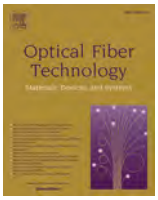

An ultra-high extinction ratio broadband photonic crystal fiber splitter designed for the terahertz band

Chao Liu [a,*], Yuan Sun [a], Yanshu Zeng [a], Wei Liu [a], Jingwei Lv [a], Lin Yang [a], Jianxin Wang [a], Qiang Liu [a], Paul K. Chu [b]

[a] School of Physics and Electronic Engineering, Northeast Petroleum University, Daqing 163318 PR China
[b] Department of Physics, Department of Materials Science and Engineering, and Department of Biomedical Engineering, City University of Hong Kong, Tat Chee Avenue, Kowloon, Hong Kong, China

ARTICLE INFO

Keywords:
Photonic crystal fiber
Polarization beam splitter
Terahertz
Coupling length

ABSTRACT

Terahertz (THz) polarization beam splitters (PBS) are valuable for applications in areas such as wireless high-speed communications and terahertz imaging. In this paper, a dual-core terahertz photonic crystal fiber (PCF) polarization beam splitter is proposed to achieve short length, high extinction ratio and wide bandwidth. This PBS has a cyclic olefin copolymer (COC) as the base material, and the dual-core structure is realized by introducing a central air hole. Performance analysis, conducted using the finite element method, reveals that the proposed PBS achieves a minimum length of 29.50688 mm, a bandwidth of 0.19 THz between 0.47 THz and 0.66 THz, and a maximum extinction ratio of −324.257 dB at an incident light frequency of 0.54 THz, where the two polarization modes are nearly completely separated. In addition, the PBS exhibits good manufacturing tolerances with a structural error of ± 1 %. These excellent properties indicate that THz PCF-PBS has great potential for applications in terahertz-band optical communication, optical sensing and optoelectronic detection.

1. Introduction

The terahertz (THz) band refers to frequencies between 0.1 terahertz and 10 terahertz [1], and is widely used in fields such as communications, imaging, and information technology [2–7]. Optical devices such as polarization control devices, polarization beam splitters, and polarization converters are also being developed for this band [8–10]. Among them, polarization beam splitters (PBS) have attracted much attention because of their ability to be integrated with a variety of terahertz devices, such as terahertz waveguides, terahertz filters, and terahertz communication devices [11–13]. Polarization beam splitters can decompose an incident beam into two mutually orthogonal beams of linearly polarized light propagating along different paths [14], which is very important for improving the accuracy and quality of signal transmission. Traditional polarization beamsplitters, such as Wollaston prism polarization beamsplitters, use birefringent crystals, which can achieve the modulation of polarized light at a specific angle, but they are large in size, not easy to be integrated, and have high requirements on the environment in which the materials are used [15]. In contrast, photonic crystal fiber (PCF) based PBS solves the shortcomings of traditional PBS. PCF not only has a flexible and adjustable structure and a wide range of communication [16,17], but also has the advantages of low loss and low dispersion in the terahertz wavelength band, which is conducive to miniaturization and integration with the optical path [18–20]. Currently, researchers have mainly studied PCF-PBS in the near- or mid-infrared wavelength band and achieved considerable results. For example, Chen et al. proposed a compact all-fiber polarizing beam splitter based on a dual-core photonic crystal fiber and an elliptical gold layer with a minimum length of 0.122 mm, a maximum extinction ratio of −65 dB at 1.55 μm, and an operating bandwidth of 100 nm [21]. Zou et al. proposed a silver-plated Zou et al. proposed a silver-plated dual-core photonic crystal fiber PBS with extinction ratios of 67.4 dB and 67.1 dB at wavelengths of 1.14 and 1.57 μm, respectively, and a length of only 17.17 μm [22]. However, in the study of THz-band PBS, there are still problems such as low precision of the micro-nano fabrication process, low material suitability, and limited bandwidth expansion. Therefore, designing a THz polarization beam splitter with excellent performance has been a hot research topic in recent years.

A number of PCF-PBSs in the THz band have been proposed. a novel cyclic olefin copolymer-based TPBS with a cascaded hexagonal porous

* Corresponding author.
E-mail address: msm-liu@126.com (C. Liu).

https://doi.org/10.1016/j.yofte.2025.104136
Received 16 August 2024; Received in revised form 25 December 2024; Accepted 8 January 2025

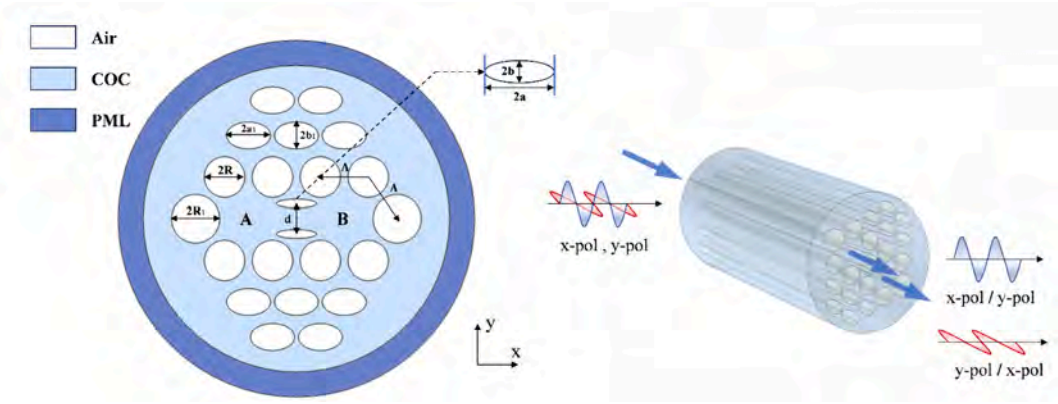

(a) (b)

Fig. 1. (a) Cross-section of the THz PCF- PBS and (b) PBS operation principle.

dual-core structured photonic crystal fiber with maximum extinction ratios of 114.5 dB and 72.3 dB, and bandwidths of 227.8 and 147 GHz for the x- and y-polarized fundamental modes, respectively, have been proposed by Miao et al., and the length of the proposed PBS is 11.655 mm [23]. Sun et al. demonstrated a terahertz wave polarization beam splitter using a full bandgap photonic crystal. This structure splits the Transverse Electric (TE) and Transverse Magnetic (TM) polarization modes into different propagation directions with extinction ratios greater than 20 dB in the frequency range of 1.225 to 1.260 THz [24]. Although these PBSs have a wide bandwidth, they require high precision of the structure and are prone to dimensional deviations during processing [25]. To address this problem, some researchers have also made improvements. Esam A.A. Hagras et al. designed and analyzed a compact terahertz dual-core photonic crystal fiber (THz-DC-PCF) polarization beam splitter. This PBS uses easy-to-machine periodic circular air holes with birefringent liquid crystals (NLCs) of type E7 permeating the double core, allowing high birefringence between the two polarization modes. The maximum extinction ratio is −62 dB, the bandwidth reaches 58 GHz, and the device length of the proposed PBS is 3.848 cm [26]. Saleki et al. proposed a tunable TPBS, this PBS employs graphene nanolayers and achieves an extinction ratio of $>$ 200 dB for TM waves with frequency f $<$ 2 THz [27]. A microstructured birefringent gradient-core polyethylene photonic crystal fiber polarizing beamsplitter was presented by Vikas Kumar et al. Their numerical analysis showed extinction ratios of −38 to −49 dB and −15 to –23 dB for x-polarization and y-polarization, respectively, for lengths ranging from 1.96 cm to 60 cm and frequencies ranging from 0.4 to 1.0 THz. The transmission loss at 1 THz is 0.05 dB/m when the bending radius is 1 cm [28]. These PBSs have simpler structures, but employ less adaptable materials and device lengths are typically centimeter-scale. Although the above PBSs show their respective advantages, there is still less research in realizing devices with both structural simplicity and high performance. Therefore, it is important to design a high-performance polarization beam splitter with short length, high extinction ratio, and wide bandwidth with simple structure.

In this paper, a dual-core PCF-PBS based on cyclic olefin copolymer (COC) is proposed. The structure employs periodically arranged air holes, and the effects of the structural parameters of the TPBS on the performance are analyzed in depth using the finite-element method, focusing on the coupling length, extinction ratio and bandwidth. The numerical results show that the extinction ratio reaches −324.257 dB when the device length is 29.50688 mm, and the operating frequency ranges from 0.47 THz to 0.66 THz, obtaining a bandwidth of 0.19 THz. The proposed PBS not only meets the requirements of short length, high extinction ratio and wide bandwidth, but its simple periodic arrangement of air holes significantly reduces the fabrication complexity compared with compact structures. It has important application prospects in terahertz-band optical communication, optical sensing and Internet information technology.

2. Structure and principle of the THz PCF-PBS

Fig. 1(a) depicts the cross-section of the PCF-PBS, where the light blue area is made of TOPAS, the white area is the air holes, and the outer dark blue ring is the perfectly matching layer. The air holes inside the fiber are periodically arranged in a diamond shape, and the two elliptical air holes in the center divide the PBS into two cores, resulting in a double-core structure. This design increases the asymmetry of the structure and improves the birefringence. The two cores are denoted by A and B, respectively. TOPAS cyclic olefin copolymer has low material dispersion in the 0.1–1.5 terahertz range with a constant refractive index of 1.525, small material loss, low water absorption, and high chemical resistance to common solvents [29]. Therefore, TOPAS is used to fabricate the PBS. The relationship between the refractive index and wavelength of COC is described by the Sellmeier equation [30]:

$$n^2(\lambda) = A_1 + \frac{(A_2\lambda^2)}{(\lambda^2 - A_3^2)} \tag{1}$$

where λ is the wavelength of the incident light, $A_1 = 2.045$, $A_2 = 0.266$, and $A_3 = 0.206$.

The coupling length (CL) describes the shortest transmission distance over which energy exchange occurs between the two cores of the beam splitter. When the energy of polarized light from one core is coupled with another, the optical energy in that core changes from maximum to minimum, while the corresponding optical energy in the other core changes oppositely. The transmission distance of the polarized light in the fiber is defined as the coupling length of the fiber, and the coupling lengths for x-polarized light and y-polarized light are expressed as follows [31]:

$$L_{x,y}^{\lambda} = \frac{\lambda}{2|n_{x(y)}^{e} - n_{x(y)}^{o}|} \tag{2}$$

where the denominator shows the effective refractive index difference between the pair of super modes for x and y-polarization. The coupling length ratio (CLR) is described by the ratio of L_x to L_y [32]:

$$CLR = \frac{L_y}{L_x} = \frac{m}{n} (m = 1, 2; n = 1, 2) \tag{3}$$

where m and n are positive integers. The optimal properties of the PBS are achieved for $L = mL_x = nL_y$ and CLR is equal to 2 or 1/2 with complete separation of the x and y polarization directions.

When x-polarization and y-polarization are coupled to the A-core,

the output power of A-core is shown in the following [33]:

$$\begin{cases} P_A^x = P_0^x cos^2(\frac{\pi}{2}\frac{L}{L_c^x}) \\ P_A^y = P_0^y cos^2(\frac{\pi}{2}\frac{L}{L_c^y}) \end{cases} \tag{4}$$

where P_0^x and P_0^y are the input powers for the x-polarized and y-polarized modes, P_A^x and P_A^y are the output powers for the x-polarized and y-polarized modes, and L is the length of the transmission device. Similarly, the output power of B-core is [34]:

$$\begin{cases} P_B^x = P_0^x - P_A^x \\ P_B^y = P_0^y - P_A^y \end{cases} \tag{5}$$

By normalizing the incident optical power, when$P_0 = 1$, the normalized power (NP) is [35]:

$$NP = \frac{P_{A,B}^{x,y}}{P_0^{x,y}} = P_{A,B}^{x,y} \tag{6}$$

In order to objectively evaluate the performance of the PBS, an extinction ratio (ER) parameter is defined to describe the degree of separation of the two orthogonally polarized components at the PBS output. It is expressed as the logarithmic ratio of the optical power of the two polarization states at the output of the PBS to gauge the ability to suppress the optical signal in different polarization states [36]. Complete separation of the two different polarization states can be attained when the absolute value of ER is greater than 20 dB:

$$\begin{cases} ER_A = 10log_{10}\frac{P_A^x}{P_A^y} \\ ER_B = 10log_{10}\frac{P_B^x}{P_B^y} \end{cases} \tag{7}$$

The finite element method (FEM) based on COMSOL Multiphysics combined with perfectly matching layers (PML) is adopted to analyze the properties of the PCF-PBS [37]. Because the fineness of the grid dissection affects the accuracy of the calculation and runtime, the grid size needs to cater to the specific situation. In order to ensure the convergence of the simulation results, the grid size and PML parameters are optimized. A grid size of $\lambda/6$ is used for COC and PML, and a fine grid size of $\lambda/4$ is used for all the pores.

In the terahertz band, the main transmission losses in photonic crystal fibers are the effective material absorption loss and confinement loss. The material absorption loss is caused by the absorption of light by the high refractive index substrate during transmission as shown in the following [38]:

$$\alpha_{neff} = \frac{1}{2}\sqrt{\frac{\varepsilon_0}{\mu_0}}\frac{\int_{A_{mat}} n\alpha_{mat}|E|^2 dA}{\left|\int_{All} S_Z\right| dA} \tag{8}$$

$$S_Z = \frac{1}{2} \times \mathrm{Re}(E \times H^*)z \tag{9}$$

where ε_0 and μ_0 are the dielectric constant and magnetic permeability in vacuum, respectively, α_{mat} is the bulk material absorption loss with a value of 0.06 cm^{-1} for the cyclic olefin copolymer COC at 0.4 THz, with an increase of 0.36 /(cm·THz), S_Z is the z-component of the Poynting vector expressed in equation (9), E is the electric field, and H is the magnetic field [39]. Integration of the numerator is performed over the region of COC, and that of the denominator part is performed over the entire region. A portion of the light propagating in a photonic crystal fiber leaks into the cladding. Since the cladding cannot be infinite, some of the energy will inevitably be lost during transmission, resulting in a confinement loss [40]:

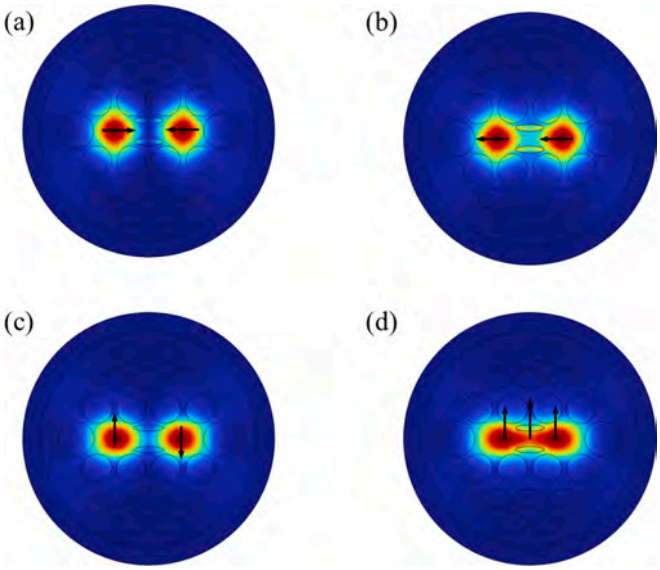

Fig. 2. (a) x polarization odd mode, (b) x polarization even mode, (c) y polarization odd mode, and (d) y polarization even mode.

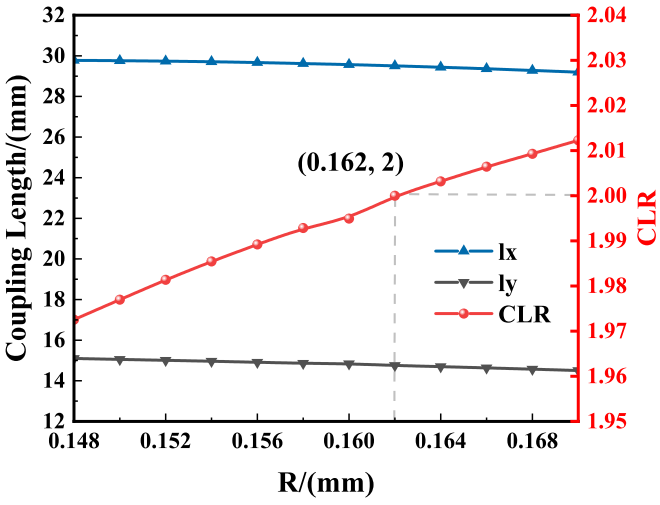

Fig. 3. Radii of circular hole versus CLR and coupling lengths.

$$\alpha_c = \frac{20}{\ln 10}\frac{2\pi}{\lambda}\mathrm{Im}(n_{eff}) = 8.686 \times \frac{2\pi f}{c}\mathrm{Im}(n_{eff}) \tag{10}$$

where f is the operating frequency and $\mathrm{Im}(n_{eff})$ is the imaginary part of the effective refractive index.

3. Simulation and analysis

According to the mode coupling theory, there are four modes in the dual-core PCF, x odd mode, x even mode, y odd mode, and y even mode. The odd mode has opposite electric field directions in the two cores, while the even mode has the same electric field direction in the two cores, as shown by Fig. 2(a) and 2(b) for the odd–even modes in the x-polarization direction and Fig. 2(c) and 2(d) for the odd–even modes in the y-polarization direction. It can be seen that most of the optical field energy is confined within the fiber core.

The inner air hole radius (R), large air hole radius (R_1), and inner elliptical air hole to core distance (d) affect the mode field distribution of the core base mode and the PBS properties. Here, we focus on the effects of these three important parameters and perform optimization, because

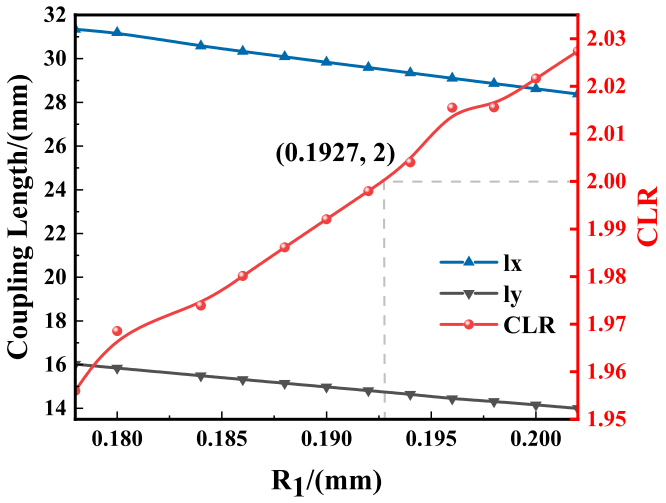

Fig. 4. Large circular hole radii versus CLR and coupling lengths.

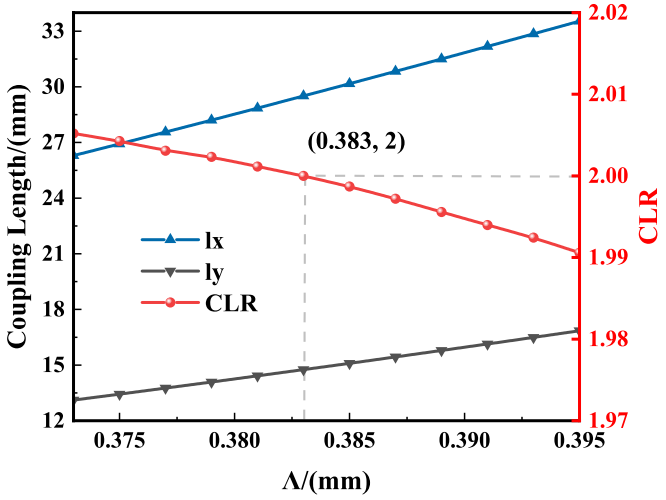

Fig. 5. Stomatal spacing as a function of CLR and coupling length.

the other parameters, such as the size and spacing of the cladding pores, have little influence. The initial parameters are $R = 0.162$ mm, $R_1 = 0.1927$ mm, $d = 0.12$ mm, $\Lambda = 0.383$ mm, $a = 0.161$ mm, $b = 0.035$ mm, $a_1 = 0.176$ mm, and $b_1 = 0.108$ mm.

While the other parameters are kept constant, Fig. 3 shows the relationship between the inner layer circular aperture R and the coupling lengths lx, ly, and CLR at 0.54 THz. Since the optical field energy leaks easily into the cladding layer when the circular hole R is smaller than 0.148 mm, and the air hole spacing is too small for manufacturing when it is larger than 0.17 mm, we choose to optimize R between 0.148 ~ 0.17 mm and obtain the result of CLR infinitely close to 2. The blue line in Fig. 3 indicates the coupling length in the x-polarization direction, the black line indicates the coupling length in the y-polarization direction, and the red line indicates the coupling length ratio. It can be observed that lx is larger than ly, revealing that the y-polarization direction exhibits a better coupling effect. As R increases, lx and ly decrease gradually, and CLR is improved, indicating that the larger the radius of the circular aperture, the easier light gathers in the fiber core and the better the coupling effect. When R is 0.162 mm, CLR is close to 2 and the properties of the PBS is better. Consequently, $R = 0.162$ mm is the optimal radius of the circular hole.

Fig. 4 shows the relationship between R_1 and the coupling lengths lx, ly, and CLR for a large circular hole on both sides at a frequency of 0.54 THz. By optimizing R_1 between 0.178 ~ 0.202 mm, lx decreases from 31.34 mm to 28.38 mm and ly from 16.02 mm to 13.99 mm with increasing R_1. lx and ly decrease with increasing R_1, and the CLR rises. When R_1 is 0.1927 mm, CLR is close to 2 and the properties of the PBS are better. Therefore, $R_1 = 0.1927$ mm is the optimal radius of the large circular hole.

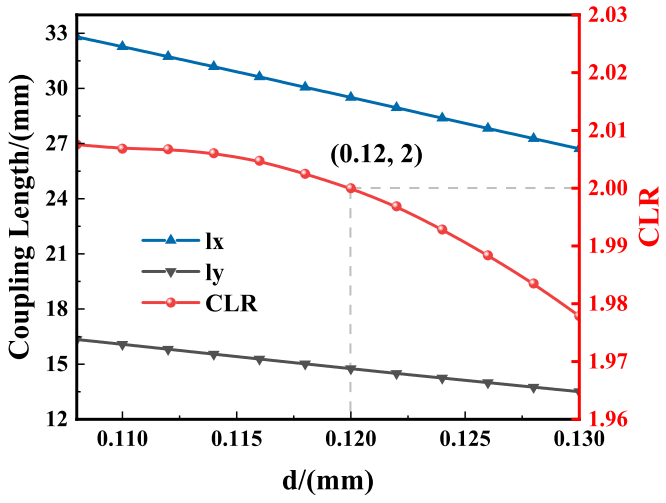

Fig. 6. Ellipse distance from the center versus CLR and coupling lengths.

Fig. 5 shows the stomatal spacing Λ versus the coupling lengths lx, ly, and CLR at 0.54 THz. By optimizing Λ between 0.373 ~ 0.395 mm, lx increases from 26.29 mm to 33.53 mm and ly from 13.11 mm to 16.84 mm with increasing Λ. lx and ly increase with increasing Λ, and CLR shows a decreasing trend, disclosing that as the stomatal distance increases, the distance of stomata from the center increases and the coupling effect decreases subsequently. When Λ is 0.383 mm, CLR is close to 2 and the properties of the PBS are better. Therefore, $\Lambda = 0.383$ mm is the optimal stomatal distance.

Fig. 6 shows the ellipse-to-center distance d versus the coupling length lx, ly, and CLR at 0.54 THz. By optimizing d between 0.108 ~ 0.13 mm, lx decreases from 32.8 mm to 26.71 mm and ly from 16.33 mm to 13.05 mm as d increases. lx and ly decrease with increasing d, and CLR shows a decreasing trend. Hence, as the center distance d increases, the distance between the elliptical air holes and the center increases. Light cannot be confined well in the core, and the coupling effect decreases. When d is 0.12 mm, CLR is close to 2 and the characteristics of the PBS are better. Therefore, $d = 0.12$ mm is the optimal air-hole spacing.

The elliptical air holes break the asymmetry of the structure and enhance the birefringence. Fig. 7(a) shows the central elliptical long axis a versus the coupling lengths lx, ly, and CLR at 0.54 THz frequency. By optimizing between 0.149 ~ 0.171 mm, lx increases from 27.14 mm to 37.53 mm and ly from 14.09 mm to 15.29 mm. lx and ly increase with increasing a. The coupling length in the x-polarization direction increases significantly with the increase in the long axis a, but the increase in the y-polarization direction is very small, implying that the long axis a does not have a significant effect on the birefringence in the y-polarization direction. When a is 0.161 mm, CLR is close to 2 and the properties of the PBS are better. Hence, $a = 0.161$ mm is the optimal stomatal spacing. Fig. 7(b) presents the relationship between the short axis b of the central ellipse and the coupling lengths lx, ly, and CLR at 0.54 THz. By optimizing b between 0.03 ~ 0.041 mm, lx increases from 26.72 mm to 34.32 mm and ly from 13.07 mm to 17.05 mm with increasing b, while lx and ly show an increasing trend with increasing b, indicating that the elliptical air holes are closer to the core. Light is confined tightly within the core, and coupling is enhanced. When b is 0.035 mm, CLR is close to 2 and the PBS characteristics are. Therefore, $b = 0.035$ mm is the optimal air-hole spacing.

The variation of CL with frequencies of the optimized PBS is shown in Fig. 8(a). As the frequency rises from 0.42 THz to 0.66 THz, lx and ly

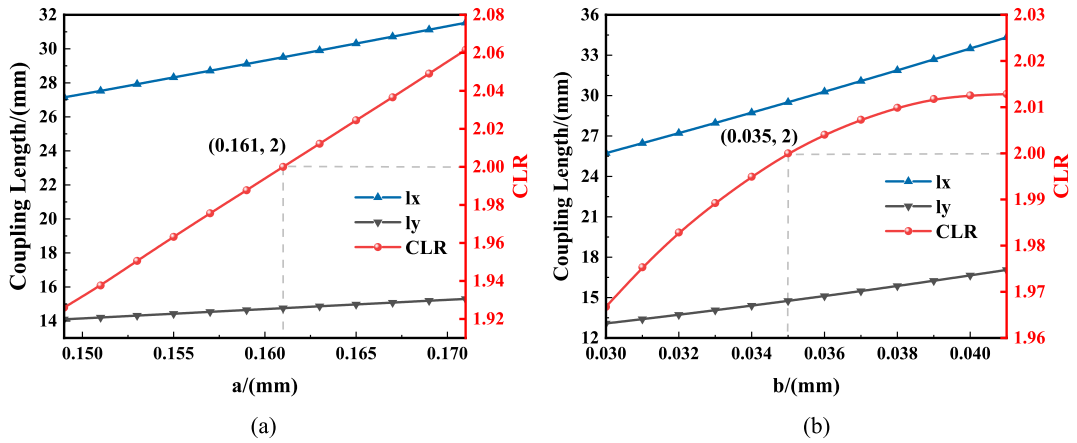

Fig. 7. (a) Long axis of the ellipse versus CLR and coupling length and (b) Short axis of the ellipse.

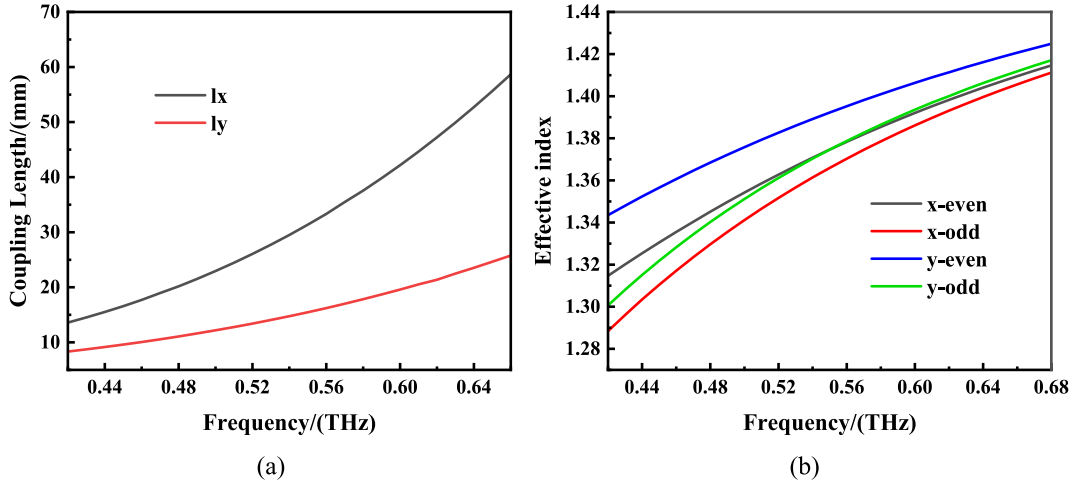

Fig. 8. (a) Coupling length versus frequency and (b) Effective refractive indexes versus frequencies for the four super modes.

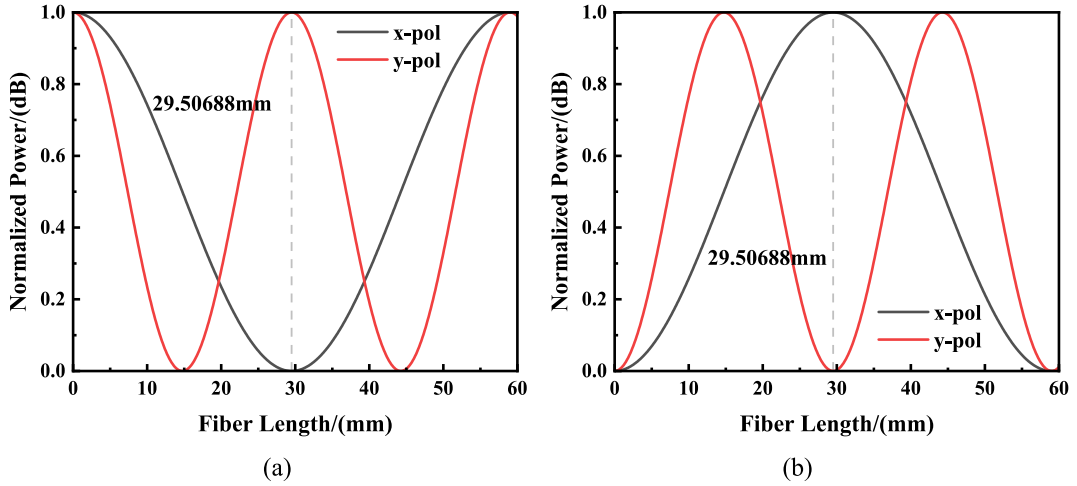

Fig. 9. (a) A-core x-polarized and y-polarized states normalized output power versus fiber length and (b) B-core.

increase. The increase of *lx* is larger than that of *ly*, because the larger the frequency, the smaller the difference of effective refractive indexes between the odd and even modes. As shown in Fig. 8(b), the effective refractive indexes of the four super modes increase with frequencies due to the asymmetry of the PCF-PBS. The effective refractive indexes of the four super models are different, indicating that the y parity mode is larger than the x parity mode and approaches unity with increasing frequencies.

Fig. 9(a) and (b) show the variation of the normalized power versus transmission distance for the dual-core x-polarized and y-polarized

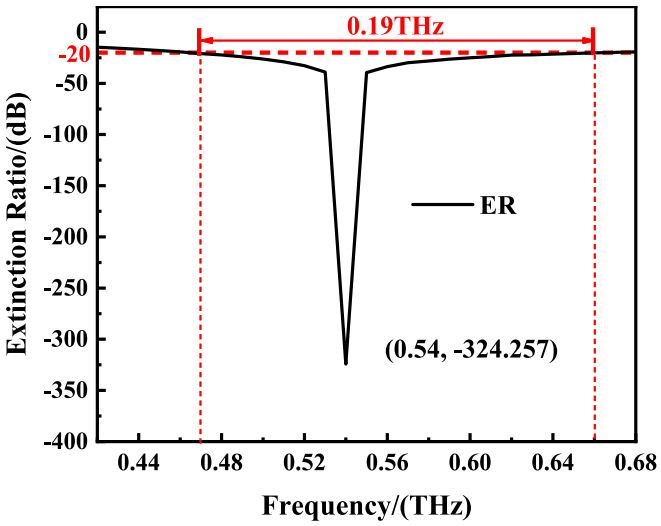

Fig. 10. ER of PBS as a function of wavelength after optimization.

modes, respectively. The normalized power between the x-polarized and y-polarized modes varies periodically with the transmission length. However, the normalized power between x-polarization and y-polarization is not synchronized due to birefringence caused by the structural asymmetry. According to Fig. 9(a), the two polarization modes are almost completely separated when $L = 29.50688$ mm $= 2\,lx = ly$, while the same conclusion is observed from Fig. 9(b), showing that B-core is the same as A-core. That is, $L = 29.50688$ mm is the shortest length that satisfies the beam-splitting condition. By separating these two polarization modes periodically, the cycle length is consistent with the minimum working length of the PBS.

Fig. 10 shows the extinction ratios versus frequencies for the polarizing beam splitter with a length of 29.50688 mm. The extinction ratio is as high as −324.257 dB at 0.54 THz. At this time, the polarized light in the two directions is almost separated completely, and the output power of y-polarized light is smaller than that of x-polarized light. When $|ER| \geq 20$ dB, the bandwidth is 0.19 THz (0.47 THz ~ 0.66 THz).

4. Discussion

The confinement losses and effective material losses with frequencies for the four polarization modes are shown in Fig. 11(a). The confinement losses of all four polarization modes decrease with increasing frequencies and level off after 0.5 THz. At 0.54 THz the total loss is 0.3051 × 10^{-9} dB/cm because the effective mode area increases with frequencies and more power leaks into the cladding. Fig. 11(b) depicts the relationship between EML and frequency. The EML values of the four polarization modes are not the same at the same frequencies, but are within a small range. The EML in the frequency range of 0.47 ~ 0.58 THz is neglected because a smaller loss can be obtained in the low-frequency region (0.1 ~ 1 THz).

Since different air pore arrangements affect the PBS properties, different air pore arrangements are studied, as shown in Fig. 12(c), in which I to III are air pores with different numbers of layers, IV is a compact air pore, and V is a sparser circular arrangement. Fig. 12(d) shows the four super modes with different structures, in which the circularly arranged sparse air holes cannot completely separate the two polarized beams and fail to achieve the basic beam-splitting function, because the optical energy leaks into the cladding part. As shown in Fig. 12(a), the blue line presents the optimal structural parameters, and the rest of the ER is far from the optimal −324.257 dB at the center frequency of 0.54 THz. Fig. 12(b) compares the coupling length ratios of different structures. The CLR of IV is as high as 2.06, and the ERs of I and III are very small. The bandwidth is short, although their coupling ratios are closer to two. The CLR after optimization is equal to 2. ER is high and the bandwidth is large. Therefore, I to V are not optimal structures, and the structure of the outer air holes is determined.

It is necessary to determine the tolerances in actual manufacturing. By taking into account the various engineering factors in the actual production and fabrication, the effects of ± 1 % variations of the optimal parameters (a, b, d, and Λ) on the PBS characteristics are shown in Fig. 13. Fig. 13(a) shows the relationship between different long and short axes a and b of the ellipse with respect to ER and bandwidth. The blue line is the ER curve under ideal conditions. It can be seen that a and b maintain a wide bandwidth of 0.019 THz (0.47 THz ~ 0.66 THz) with an error of ± 1 %, so the effect of the preparation tolerance on the bandwidth is minimal. When it is increased to 1 + 1 %, the maximum ER is −280.549 dB as shown by the red line in the figure, which is about 13.46 % lower than that of the ideal ER. The maximum ER is much less than −20 dB at 0.54 THz when b is varied at 1 ± 1 %, as shown by the green curve and the yellow dashed line, still reflecting good beam-

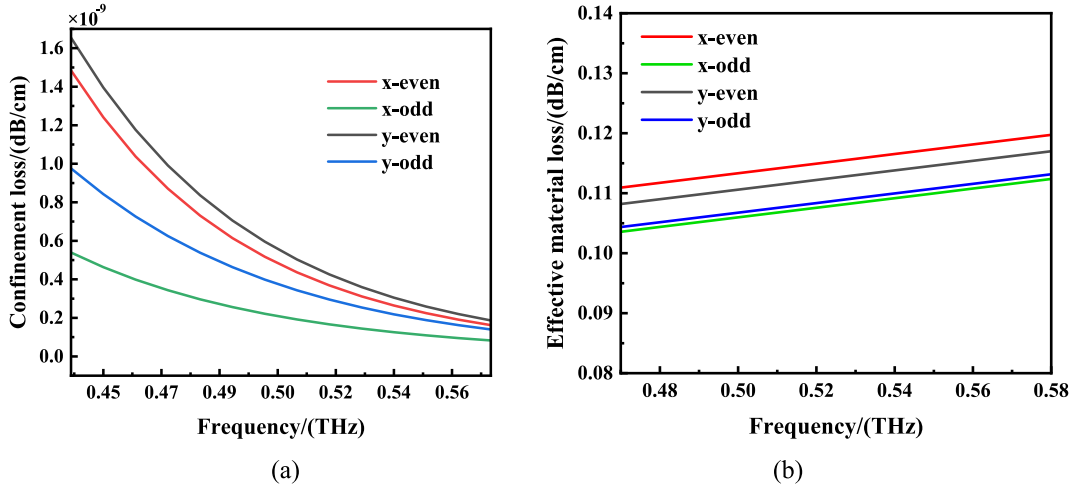

Fig. 11. (a) Constraint loss versus frequency for x-polarized and y-polarized odd and even modes and (b) Effective material loss versus frequency for x-polarized and y-polarized odd and even modes.

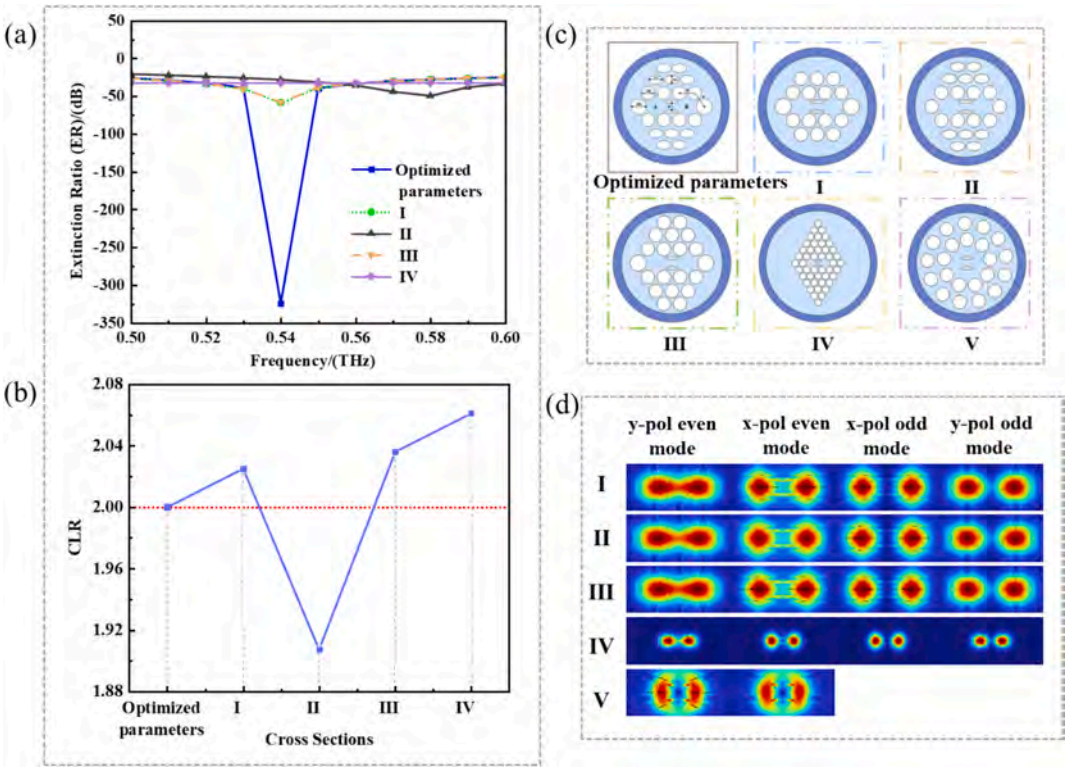

Fig. 12. (a) ER versus frequency for different aperture arrangements, (b) Comparison of CLR for different aperture arrangements, (c) Fiber cross-section for different aperture arrangements, and (d) Four super modes with different aperture arrangements.

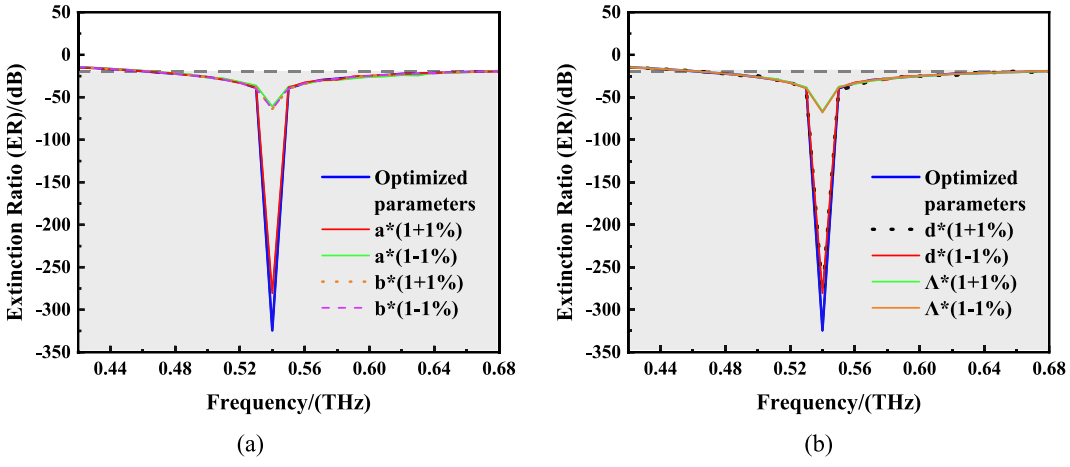

Fig. 13. (a) a, b ± 1 % manufacturing tolerance and (b) d, Λ ± 1 % preparation tolerance.

splitting characteristics. Fig. 13(b) shows the effects of the ellipse distance from the center spacing d and stomatal spacing Λ on the ER and bandwidth. The bandwidth remains constant. When d has a 1 ± 1 % error, the maximum ER is −280.874 dB, as indicated by the red and black dashed lines. Similarly, the maximum ER is obtained when Λ is varied at ± 1 % at 0.54 THz. Although the variation of the structural parameters during manufacturing affects the extinction ratio, |ER| at 0.54 THz is still much larger than 20 dB, and the bandwidth is almost unaffected. All in all, the results show that the PCF-PBS has good fabrication tolerances.

Table 1 compares the performance of the THz PCF-PBS with that of the current state-of-the-art TPBS by listing the device length, maximum extinction ratio, and bandwidth. It shows that our PBS achieves not only an ultra-wide bandwidth of 0.19 THz from 0.47 THz to 0.66 THz, but also an extinction ratio of −324.257 dB.

Table 1
Comparison of the properties of our PCF-PBS and those of similar state-of-the-art beam splitters.

Structure	Beam Splitter Length(mm)	Maximum ER (dB)	Bandwidth (THz)	References
	45.16	107.7	0.02	[41]
	53.88	114.5	0.0217	[42]
	12.7	−20	0.046	[43]
	109	65	0.015	[44]
	23.51	−324.257	0.19	This work

5. Conclusion

In this paper, a COC-based THz dual-core PCF-PBS is proposed. This PBS enhances the structural asymmetry and improves the device birefringence by introducing two elliptical air holes in the fiber core. By optimizing the size and spacing of these air holes, the PBS achieves an ultrashort length of 29.50688 mm, a wide bandwidth of 0.19 THz between 0.47 THz and 0.66 THz, and an exceptional extinction ratio of −324.257 dB at 0.54 THz, where the polarization modes are effectively separated. In addition, in order to demonstrate the high preparation tolerances, the performance of the PBS was analyzed with a ± 1 % change in the structural parameters, and it was found that the bandwidth of PBS is almost unaffected and the ER remains good.Compared with other THz-PBSs, the proposed PBS simultaneously satisfies the three key requirements of ultrashort length, high ER, and wide bandwidth, which provides a new idea for realizing miniature polarization devices in the terahertz field.

CRediT authorship contribution statement

Chao Liu: Writing – review & editing, Validation, Supervision, Resources, Project administration, Methodology, Investigation, Formal analysis, Data curation, Conceptualization. **Yuan Sun:** Writing – review & editing, Writing – original draft, Validation, Supervision, Software, Methodology, Investigation, Formal analysis, Data curation, Conceptualization. **Yanshu Zeng:** Writing – review & editing, Validation, Supervision, Formal analysis, Data curation, Conceptualization. **Wei Liu:** Validation, Supervision, Formal analysis, Data curation, Conceptualization. **Jingwei Lv:** Visualization, Validation, Supervision, Formal analysis, Conceptualization. **Lin Yang:** Validation, Supervision, Investigation, Conceptualization. **Jianxin Wang:** Validation, Supervision, Methodology, Conceptualization. **Qiang Liu:** Validation, Supervision, Methodology, Conceptualization. **Paul K. Chu:** Writing – review & editing, Validation, Supervision, Conceptualization.

Declaration of competing interest

The authors declare that they have no known competing financial interests or personal relationships that could have appeared to influence the work reported in this paper.

Acknowledgments

This work was jointly supported by the Heilongjiang Provincial Natural Science Foundation of China [JQ2023F001], National Natural Science Foundation of China [12304480], Local Universities Reformation and Development Personnel Training Supporting Project from Central Authorities, Natural Science Foundation of Heilongjiang Province [LH2021F007], China Postdoctoral Science Foundation funded project [2020 M670881], as well as City University of Hong Kong Donation Research Grants [9220061 and DON-RMG 9229021].

Data availability

Data will be made available on request.

References

[1] C. Chaccour, M.N. Soorki, W. Saad, M. Bennis, P. Popovski, M. Debbah, Seven defining features of terahertz (THz) wireless systems: a fellowship of communication and sensing, IEEE Commun. Surv. Tut. 24 (2) (2022) 967–993, https://doi.org/10.1109/COMST.2022.3143454.
[2] W. Jiang, Q. Zhou, J. He, M.A. Habibi, S. Melnyk, M. El-Absi, V.C. Leung, Terahertz communications and sensing for 6G and beyond: a comprehensive review, IEEE Commun. Surv. Tut. 26 (4) (2024) 2326–2381, https://doi.org/10.1109/COMST.2024.3385908.
[3] N. Yang, A. Shafie, Terahertz communications for massive connectivity and security in 6G and beyond era, IEEE Commun. Mag. 62 (2) (2024) 72–78, https://doi.org/10.1109/MCOM.001.2200421.
[4] W.J. Choi, S.H. Lee, M.N.A. ChaKotov, Chiral Kirigami for bend-tolerant reconfigurable hologram with continuously variable chirality measures, Adv. Mater. 36 (30) (2024) 2401131, https://doi.org/10.1002/adma.202401131.
[5] A.G. Markelz, D.M. Mittleman, Perspective on terahertz applications in bioscience and biotechnology, ACS Photonics 9 (4) (2022) 1117–1126, https://doi.org/10.1021/acsphotonics.2c00228.
[6] Y. Jiang, G. Li, H. Ge, F. Wang, L. Li, X. Chen, M. Lu, Y. Zhang, Machine learning and application in terahertz technology: a review on achievements and future challenges, IEEE Access 10 (2022) 53761–53776, https://doi.org/10.1109/ACCESS.2022.3174595.
[7] Y. Cui, Y. Xu, D. Han, X. Wang, Z. Shen, Y. Hou, X. Chen, Hidden-information extraction from layered structures through terahertz imaging down to ultralow SNR, Sci. Adv. 9 (40) (2023) 8435, https://doi.org/10.1126/sciadv.adg8435.
[8] J. Lv, W. Li, J. Wang, X. Lu, Q. Li, Y. Ren, C. Liu, High-sensitivity strain sensor based on an asymmetric tapered air microbubble Fabry-Pérot interferometer with an ultrathin wall, Opt. Express 32 (11) (2024) 19057–19068, https://doi.org/10.1364/OE.521356.
[9] W. Deng, L. Chen, H. Zhang, S. Wang, Z. Lu, S. Liu, X. Zhang, On-chip polarization- and frequency-division demultiplexing for multidimensional terahertz communication, Laser Photonics Rev. 16 (10) (2022) 2200136, https://doi.org/10.1002/lpor.202200136.
[10] J. Lv, Y. Ren, D. Wang, J. Wang, X. Lu, Y. Yu, C. Liu, Optical switching with high-Q Fano resonance of all-dielectric metasurface governed by bound states in the continuum, Opt. Express 32 (16) (2024) 28334–28347, https://doi.org/10.1364/OE.530788.
[11] B. Chen, K. Zhou, J. Shao, X. Zhao, B. Xu, J. Zhu, C. Wu, A low-loss hollow-core waveguide bundle for terahertz imaging under a cryogenic environment, ACS Photonics 11 (2024), https://doi.org/10.1021/acsphotonics.4c00310.
[12] Z. Tian, Z. Luo, X. Lv, M. Xie, G. Peng, D. Kong, H. Guan, Tunable band-stop fiber filter based on laser-induced graphene metamaterial in THz frequency, Opt. Express 32 (14) (2024) 24251–24261, https://doi.org/10.1364/OE.527472.
[13] W. Gao, M. Fujita, S. Murakami, T. Nagatsuma, C. Fumeaux, W. Withayachumnankul, Ultra-wideband terahertz integrated polarization multiplexer, Laser Photonics Rev. 11 (4) (2024) 2400270, https://doi.org/10.1002/lpor.202400270.
[14] H. Wu, Y. Tan, D. Dai, Ultra-broadband high-performance polarizing beam splitter on silicon, Opt. Express 25 (6) (2017) 6069–6075, https://doi.org/10.1364/OE.25.006069.
[15] J. Zhu, Y. Yang, D. McGloin, S. Liao, Q. Xue, Sub-terahertz 3-D printed all-dielectric low-cost low-profile lens-integrated polarization beam splitter, IEEE Trans Terahertz Sci. Technol. 11 (4) (2021) 433–442, https://doi.org/10.1109/TTHZ.2021.3064209.
[16] W. Liu, Y. Shi, Z. Yi, C. Liu, F.M. Wang, X.L. Li, J.W. Lv, L. Yang, P.K. Chu, Surface plasmon resonance chemical sensor composed of a microstructured optical fiber for the detection of an ultra-wide refractive index range and gas-liquid pollutants, Opt. Express 29 (25) (2021) 40734–40747, https://doi.org/10.1364/OE.444323.
[17] W. Liu, C. Liu, J.X. Wang, J.W. Lv, Y. Lv, L. Yang, N. An, Z. Yi, Q. Liu, C.J. Hu, P. K. Chu, Surface plasmon resonance sensor composed of microstructured optical fibers for monitoring of external and internal environments in biological and environmental sensing, Results Phys. 47 (2023) 106365, https://doi.org/10.1016/j.rinp.2023.106365.
[18] L. Kong, C. Jia, Z. Di, J. Li, J. Yao, High birefringence low loss low dispersion ring core photonic crystal fiber on terahertz band, J. of Opt. Commun. (2022), https://doi.org/10.1515/joc-2022-0076.
[19] P. Zhang, C. Zhang, Y. Yang, L. Ke, B. Fang, C. Li, X. Jing, Polarization sensitive terahertz all dielectric continuous trapezoid metasurface beam splitter, Infrared

Phys. Technol. 130 (2023) 104604, https://doi.org/10.1016/j.infrared.2023.104604.
[20] J.X. Wang, X. Lu, C. Mi, Q. Yin, J.W. Lv, L. Yang, W. Liu, Z. Yi, Q. Liu, P.K. Chu, C. Liu, Ultra-high sensitivity photonic crystal fiber sensor based on dispersion turning point sensitization of surface plasmonic polariton modes for low RI liquid detection, Opt. Express 32 (19) (2024) 32895–32908, https://doi.org/10.1364/OE.531112.
[21] N. Chen, W. Yue, Y. Xu, W. Guo, Y. Xiao, C. Liu, Design and simulation of a compact polarization beam splitter based on dual-core photonic crystal fiber with elliptical gold layer, Sci. Rep. 14 (1) (2024) 18017, https://doi.org/10.1038/s41598-024-68995-3.
[22] H. Zou, J. Zhou, A. Jiang, L. Wei, Y. Lu, Y. Du, R. Zhang, D. Zhou, Ultra-broadband small-size dual-core photonic crystal fiber polarization splitter based on silver coating, Opt. Commun. 557 (2024) 130285, https://doi.org/10.1016/j.optcom.2024.130285.
[23] K. Miao, S. Xu, Compact THz polarization splitter with large bandwidth based on cascade hexagonal porous two-core PCF, Fiber Integr. Opt. 43 (6) (2024) 283–314, https://doi.org/10.1080/01468030.2024.2413403.
[24] J.Z. Sun, J.S. Li, Terahertz wave polarization splitter using full band-gap photonic crystals, J. Infrared Milli. Terahz. Waves 36 (2015) 255–261, https://doi.org/10.1007/s10762-014-0131-7.
[25] L. Wu, J. Wang, Y. Xia, Y. Li, L. Sheng, Optimization of polarization balance in beam splitter films for weak star simulator, Opt. Express 32 (14) (2024) 25304–25316, https://doi.org/10.1364/OE.528819.
[26] E.A.A. Hagras, M.F.O. Hameed, S.S.A. Obayya, Compact dual-core liquid crystal photonic crystal fiber polarization splitter for terahertz applications, Optik 265 (2022) 169396, https://doi.org/10.1016/j.ijleo.2022.169396.
[27] Z. Saleki, Y. Fang, S.R. Entezar, Broadband terahertz polarizing beam splitter based on a graphene-based defective one-dimensional photonic crystal, IEEE Photonics J. 11 (5) (2019) 1–13, https://doi.org/10.1109/JPHOT.2019.2935084.
[28] V. Kumar, R.K. Varshney, S. Kumar, Design of a compact and broadband terahertz polarization splitter based on gradient dual-core photonic crystal fiber, Appl. Opt. 59 (7) (2020) 1974–1979, https://doi.org/10.1364/AO.383915.
[29] Z. Hui, X. Yang, D. Han, F. Zhao, J. Gong, L. Gao, J. Yu, Sector-type high birefringence hollow-core anti-resonant terahertz photonic crystal fiber with low loss, Opt. Fiber Technol. 67 (2021) 102728, https://doi.org/10.1016/j.yofte.2021.102728.
[30] R. Islam, G.K.M. Hasanuzzaman, M.S. Habib, S. Rana, M.A.G. Khan, Low-loss rotated porous core hexagonal single-mode fiber in THz regime, Opt. Fiber Technol. 24 (2015) 38–43, https://doi.org/10.1016/j.yofte.2015.04.006.
[31] A. Bertoncini, C. Liberale, 3D printed waveguides based on photonic crystal fiber designs for complex fiber-end photonic devices, Optica 7 (11) (2020) 1487–1494, https://doi.org/10.1364/OPTICA.397281.
[32] J. Jia, Y. Han, Y. Wang, M. Bai, T. Dong, W. Wang, Y. Zhang, Double nested dual-core negative curvature fiber polarization beam splitter, Opt. Fiber Technol. 82 (2024) 103598, https://doi.org/10.1016/j.yofte.2023.103598.
[33] H. Jiang, E. Wang, J. Zhang, L. Hu, Q. Mao, Q. Li, K. Xie, Polarization splitter based on dual-core photonic crystal fiber, Opt. Express 22 (25) (2014) 30461–30466, https://doi.org/10.1364/OE.22.030461.
[34] H. Jia, X. Wang, B. Huang, L. Xue, X. Sheng, S. Lou, Compact single-polarization coupler based on a dual-hollow-core anti-resonant fiber, Opt. Express 31 (8) (2023) 12410–12422, https://doi.org/10.1364/OE.481891.
[35] Y. Zeng, J. Lv, L. Yang, W. Liu, Z. Yi, Q. Liu, C. Liu, Short dual-core GaAs photonic crystal fiber splitter with a broad bandwidth and ultrahigh extinction ratio, Appl. Opt. 62 (9) (2023) 2237–2244, https://doi.org/10.1364/AO.483504.
[36] Y. Su, M. Qin, M. Ouyang, L. Lei, L. He, T. Wang, T. Yu, Compact topological polarization beam splitter based on all-dielectric fishnet photonic crystals, Opt. Lett. 48 (12) (2023) 3171–3174, https://doi.org/10.1364/OL.492427.
[37] H. Zhang, X. Shi, G. Wen, T. Li, D. Jia, T. Liu, Force sensing based on distributed polarization coupling in polarization-maintaining fiber using finite element method, Opt. Fiber Technol. 58 (2020) 102290, https://doi.org/10.1016/j.yofte.2020.102290.
[38] G.K.M. Hasanuzzaman, M.S. Habib, S.A. Razzak, M.A. Hossain, Y. Namihira, Low loss single-mode porous-core kagome photonic crystal fiber for THz wave guidance, J. Lightwave Technol. 33 (19) (2015) 4027–4031, https://doi.org/10.1109/JLT.2015.2459232.
[39] L. Xue, X. Sheng, H. Jia, S. Lou, An ultra-wide single-mode frequency bandwidth and low-flattened dispersion hollow-core negative-curvature Thz waveguide, J. Lightwave Technol. 41 (18) (2023) 6043–6052, https://doi.org/10.1109/JLT.2023.3269788.
[40] B.K. Paul, K. Ahmed, Highly birefringent TOPAS based single mode photonic crystal fiber with ultra-low material loss for Terahertz applications, Opt. Fiber Technol. 53 (2019) 102031, https://doi.org/10.1016/j.yofte.2019.102031.
[41] Y. Zheng, J. Liu, Y. Wang, H. Liu, W. Wang, X. Xie, Design of compact dual-core terahertz polarization beam splitter with broad bandwidth, Microw. Opt. Techn. Let. 65 (5) (2023) 1277–1284, https://doi.org/10.1002/mop.33384.
[42] J.X. Zhang, Dual-core PCF-based THz polarization beam splitter with broad bandwidth and ultra-high extinction ratio, Optik 251 (2022) 168425, https://doi.org/10.1016/j.ijleo.2021.168425.
[43] Y.F. Zhu, X. Liu, C.F. Rao, H. Zhong, H.M. Luo, Y.H. Chen, H. Wang, Low-loss terahertz polarization splitter based on an asymmetric dual-suspended-core fiber, Opt. Eng. 57 (8) (2018) 086112, https://doi.org/10.1117/1.OE.57.8.086112.
[44] E. Reyes-Vera, J. Usuga-Restrepo, C. Jimenez-Durango, J. Montoya-Cardona, N. Gomez-Cardona, Design of low-loss and highly birefringent porous-core photonic crystal fiber and its application to terahertz polarization beam splitter, IEEE Photonics J. 10 (4) (2018) 1–13, https://doi.org/10.1109/JPHOT.2018.2860251.